Analytic kludge waveforms for extreme-mass-ratio inspirals of a charged object around a Kerr-Newman black hole

Tieguang Zi,[1,2] Ziqi Zhou,[3] Hai-Tian Wang,[4,2] Peng-Cheng Li[1,5,2,*] Jian-dong Zhang[2,†] and Bin Chen[3,5,6]

[1]*School of Physics and Optoelectronics, South China University of Technology,*
Guangzhou 510641, People's Republic of China
[2]*MOE Key Labortory of TianQin Mission, TianQin Research Center for Gravitational Physics and*
School of Physics and Astronomy, Frontiers Science Center for TianQin,
CNSA Research Center for Gravitational Waves, Sun Yat-sen University (Zhuhai Campus),
Zhuhai 519082, China
[3]*Department of Physics, Peking University, No. 5 Yiheyuan Road,*
Beijing 100871, People's Republic of China
[4]*Key Laboratory of Dark Matter and Space Astronomy, Purple Mountain Observatory,*
Chinese Academy of Sciences, Nanjing 210023, People's Republic of China
[5]*Center for High Energy Physics, Peking University, No. 5 Yiheyuan Road,*
Beijing 100871, People's Republic of China
[6]*Collaborative Innovation Center of Quantum Matter, No. 5 Yiheyuan Road,*
Beijing 100871, People's Republic of China

We derive the approximate "analytic-kludge" waveforms for the inspiral of a charged stellar-mass compact object (CO) into a charged massive Kerr-Newman black hole. The modifications of the inspiral orbit due to the charges in this system can be attributed to three sources: the electric force between the CO and the massive black holes (MBH), the energy flow of the dipole electromagnetic radiation, and the deformation of the metric caused by the charge of the MBH. All these are encoded explicitly in the fundamental frequencies of the orbits, which are calculated analytically in the weak-field regime. By calculating the mismatch between the waveforms for charged and neutral extreme-mass-ratio inspirals systems with respect to space-borne detectors TianQin and LISA, we show that tiny charges in the system can produce distinct imprints on the waveforms. Finally, we perform parameter estimation for the charges using the Fisher information matrix method and find that the precision can reach the level of 10^{-5} in suitable scenarios. We also study the effects of charges on the parameter estimation of charge, where the effects from the charge of the MBH can be well explained by its effects on the cutoff of the inspiral.

I. INTRODUCTION

Black hole (BH) no-hair theorems [1,2] imply that the astrophysical BHs in electrovacuum are described by the Kerr-Newman (KN) metric [3], which can be uniquely characterized by the mass, spin, and electric charge. It is widely believed that the astrophysical BHs have negligible electric charge, due to the neutralization by surrounding plasmas, quantum discharge effects, or electron-positron pair production [4,5]. However, unequivocally observational evidence for the neutrality of both stellar-mass and massive BHs are still lacking. Besides, some novel mechanisms have been proposed such that BHs could retain a large amount of charge. For example, relying on the well-known Wald mechanism [6] by which a spinning BH

immersed in an external magnetic field acquires a stable net charge, it was shown in [7] that a strongly magnetized neutron star in such a binary system will give rise to a large enough charge in the BH to allow for potentially observable effects. Additionally, the charge parameter in the KN metric can be regarded as the other types of charge, including magnetic charge (via duality transformation) [8,9], a vector charge in the scalar-tensor-vector gravity (also known as "MOG") [10,11], or a hidden electromagnetic charge in the minicharged dark matter model [12]. In all these cases, the BHs can be charged. Thus, the validation of tiny or null charge in black hole is essential for us to understand various problems in gravity and astrophysics, ranging from the third hair on black hole to the formation mechanism of real astrophysical BHs.

In contrast to the electromagnetic observations [13,14], gravitational wave (GW) observations offer a more robust way to place constraints on the charges, in the sense that the

*pchli2021@scut.edu.cn
†zhangjd9@mail.sysu.edu.cn

assumptions for the models used in the former usually contain more uncertainties. If BHs are indeed charged and described by the KN metric, the gravitational wave signatures from binary BHs will be modified. Recently, several works [15–21] have emerged to analyze the charges of the stellar mass BHs observed by LIGO and Virgo [22,23]. For example, by performing numerical relativity simulations of the coalescence of the charged binary BHs, the authors in Refs. [16,17] showed that GW150914 is compatible with having a charge-to-mass ratio smaller than 0.3. With the accurate quasinormal mode spectrum obtained from solving numerically the coupled perturbation equations of the KN BHs [24], Ref. [21] analyzed the ringdown signal of GW150914 and found that the charge-to-mass ratio is smaller than 0.33, by restricting the mass and spin to values compatible with the analysis of the full signal. For the future space-based GW detectors, Ref. [25] analyzed the capability of constraining the STVG parameter α with the ringdown of MBHBs, and the corresponding constraint for the charge-to-mass ratio is about 10^{-2}.

Instead of the binary BHs with comparable mass, in this work, we focus on the charge effect on the GW signals generated from the inspirals of stellar-mass compact objects (COs) into massive black holes (MBH) in galactic nuclei, i.e., the extreme-mass-ratio inspirals (EMRI) [26,27], and study the detectability of the charges of both the CO and BHs for future space-based GW detectors, such as TianQin (TQ) [28] and LISA [29]. EMRI is one of the most important sources for future space-based GW detectors, as the waveform contains a wealth of information about the spacetime geometry of BHs and the parameters of the system can be measured very accurately [30–33]. The data analysis requires the construction of accurate waveforms to enable accurate extraction of EMRI parameters from a signal.

Since the waveforms are slow-footed to calculate in the relativistic region for EMRIs, it is full of the substantial challenges to model EMRI dynamics precisely and constrain source parameters [34]. Most parameter estimations on EMRI sources adopt the "kludge" waveforms [35–37] to generate fast waveforms. In the realm of modeling EMRI, the kludge is in a way the approximative and built-up model that adopts several sets of post-Newtonian (PN) formulas to produce waveforms efficiently. The kludge waveforms can reflect the main feature of accurate EMRI waveforms, including some relativistic effects, such as orbital eccentricity and relativistic precession. Recently, the full relativistic EMRI waveforms have been developed in [38,39], which combine the speed of EMRI "kludge" models and the accuracy of the first order gravitational self-force models.

In the past decades, EMRI waveforms have been worked out in the alternative theories of gravity [40–47] to test their feasibility in the strong field region. Recently, Ref. [48]

calculated the EMRI waveform for a charged object inspiraling around a Schwarzschild BH in a circular orbit using the Teukolsky method. In this work, we would like to extend the analytic kludge (AK) method to the charged case by considering the inspiral of a charged CO into a charged MBH. From the point of view of testing the Kerr hypothesis, the KN BH can be treated as a representative model deviating from the Kerr BH, and its metric is analytically known and well behaved in the full range of the deviation parameter. In the AK model, the CO is moving on a Keplerian ellipse with the orbital parameters (semilatus rectum and eccentricity) slowly evolving under the influence of radiation reaction, and the relativistic precession of the orbital plane and the perihelion are included. All the evolution equations are obtained under the PN approximations. Then the waveform is generated with the well-known Peter-Mathews formula [49,50] in the quadrupole approximation. We will show that the introduce of charges into the EMRI will modify the precession via the fundamental frequencies of the orbits of the charged CO. Moreover, the effects of the charges on the radiation reaction are twofold: the direct modification to the loss of the energy and angular momentum due to gravitational radiation and the occurrence of electromagnetic radiation. Physically, the modifications due to the presence of the charges in this system can be attributed to the electric force between the CO and the MBH, the dipole electromagnetic radiation, and the deformation of the metric caused by the charge of the KN BH. The complete evolution equations of various orbital parameters are then obtained by combining the corrections due to the charges in the system appearing at the leading order of the PN expansion and the higher order terms from the original AK model. Furthermore, to quantify the effects of the charges on the waveforms, we will compute the mismatch between waveforms from the neutral EMRI system and the charged one. Finally, we will perform parameter estimation of the charges for the CO and MBH with space-borne GW detectors TQ and LISA.

The paper is organized as follows. In Sec. II, we present the calculation of the waveforms by following the approach of [35]. In Sec. III, we describe the formalisms of signal analysis for extracting values of the system parameters from the waveforms. In Sec. IV, we present the result of the constraints using the EMRI observation of LISA and TQ, then place the parameter estimation about charges of the CO and the MBH. Finally, we give a brief summary in Sec. V. Throughout this paper, we use the geometric units, where $c = G = 1$.

II. EMRI WAVEFORMS

A. Equations of motion

The KN BH is a stationary, axisymmetrical, and asymptotically flat solution of the Einstein-Maxwell equation. In Boyer-Lindquist coordinates, the KN metric can be written as

$$ds^2 = \frac{\Sigma}{\Delta} dr^2 + \Sigma d\theta^2 + \frac{\sin^2\theta}{\Sigma}[(r^2 + \tilde{a}^2)d\phi - \tilde{a}dt]^2 \qquad (1)$$

$$- \frac{\Delta}{\Sigma}[\tilde{a}\sin^2\theta d\phi - dt]^2, \qquad (2)$$

where

$$\Sigma(r,\theta) = r^2 + \tilde{a}^2\cos^2\theta, \qquad (3)$$

$$\Delta(r) = r^2 - 2Mr + \tilde{a}^2 + \tilde{Q}^2, \qquad (4)$$

and M and $\tilde{Q}$ are the mass and electric charge of the BH, and $\tilde{a}$ is specific angular momentum. The electromagnetic potential is given by

$$A = \frac{\tilde{Q}r}{\Sigma}(dt - \tilde{a}\sin^2\theta d\phi). \qquad (5)$$

The first-order equations of motion for a timelike charged particle with mass m and electric charge $\tilde{q}$ are given by [51]

$$\Sigma\frac{dt}{d\tau} = \frac{r^2 + M^2 a^2}{\Delta}P - a(aE\sin^2\theta - L_z)M^2, \qquad (6)$$

$$\Sigma\frac{dr}{d\tau} = \pm\sqrt{R}, \qquad (7)$$

$$\Sigma\frac{d\theta}{d\tau} = \pm M\sqrt{\Theta}, \qquad (8)$$

$$\Sigma\frac{d\phi}{d\tau} = \frac{aM}{\Delta}P - aME + \frac{ML_z}{\sin^2\theta}, \qquad (9)$$

where

$$R = P^2 - \Delta[r^2 + M^2(L_z - aE)^2 + M^2C],$$
$$\Theta = C - \left[(1 - E^2)a^2 + \frac{L_z^2}{\sin^2\theta}\right]\cos^2\theta, \qquad (10)$$

with

$$P = E(r^2 + M^2a^2) - M^2aL_z - MqQr. \qquad (11)$$

In the equations of motion, there are three constants of motion. $\tilde{E}$ and $\tilde{L}_z$ are the conserved total energy and component of angular momentum parallel to symmetry axis, respectively, and $\tilde{C}$ is the Carter constant [52]. Note that in above expressions, we have used dimensionless quantities defined by

$$E = \frac{\tilde{E}}{m}, \qquad a = \frac{\tilde{a}}{M}, \qquad q = \frac{\tilde{q}}{m}, \qquad L_z = \frac{\tilde{L}_z}{mM},$$
$$C = \frac{\tilde{C}}{m^2M^2}, \qquad Q = \frac{\tilde{Q}}{M}. \qquad (12)$$

One can see that the distinction between the above equations and the geodesic equations for a neutral particle moving in Kerr spacetime only reflects in the functions Δ and P.

B. Fundamental frequencies

In the AK model, if the spin of the CO is neglected, an EMRI event is completely specified by 14 degrees of freedom. To obtain the inspiral orbits of the charged CO in the KN background, we append two charge parameter Q and q to the original AK model parameter space, such that

$$\lambda^i \equiv [\lambda^1, ..., \lambda^{16}]$$
$$= [m, M, a, q, Q, e_{\text{LSO}}, \tilde{\gamma}_0, \Phi, \cos\theta_S, \phi_S, \cos\lambda_I, \alpha_0,$$
$$\cos\theta_K, \phi_K, D, t_0], \qquad (13)$$

where the definition and meaning of each parameter can be found in [35].

The trajectories of charged CO are roughly treated as quasi-Keplerian ellipses, which are characterized by the eccentricity e, and the radial orbital frequency ν. The instantaneous phase of the CO in the orbit is specified by the mean anomaly Φ. The orientation of the orbit is described by three angles: λ_I, the inclination angle of the orbital plane with respect to the BH's spin direction $\hat{S}$, $\tilde{\gamma}$, the angle from pericenter to $\hat{L} \times \hat{S}$, and α describing the direction of $\hat{L}$ around $\hat{S}$, where $\hat{S}$ is a unit vector of BH's spin, and $\hat{L}$ is a unit vector of the orbital angular momentum. The rate of change $\dot{\Phi}$, the orbital plane precession (also known as Lense-Thirring precession) frequency $\dot{\alpha}$, and the angular rate $\dot{\alpha} + \dot{\tilde{\gamma}}$ of periapsis precession are closely related to the fundamental frequencies of the CO's orbit by

$$\dot{\Phi} = 2\pi\nu = \Omega_r, \qquad (14)$$

$$\dot{\tilde{\gamma}} = \Omega_\theta - \Omega_r, \qquad (15)$$

$$\dot{\alpha} = \Omega_\phi - \Omega_\theta, \qquad (16)$$

where Ω_r, Ω_θ, and Ω_ϕ denote the fundamental frequencies of radial, polar, and azimuthal motion, respectively. The closed form of these fundamental frequencies for Kerr BH orbits was first obtained by Schmidt [53] by employing the elegant action-angle variable formalism of the Hamilton-Jacobi theory. Later on, combining Schmidt's description and using the Mino time [54], Drasco and Hughes [55] derived the fundamental frequencies and showed the construction of the frequency domain representation of arbitrary functions of orbits. In this work, we would like to follow the steps in [55] and also [43,56] to derive the analytical expressions of these three fundamental frequencies in the weak-field regime.

First of all, in terms of the dimensionless time variable, i.e., the so-called Mino's time [54],

$$\frac{d}{d\lambda} = \frac{\Sigma}{M}\frac{d}{d\tau}, \qquad (17)$$

the equations of motion for the charged CO now become

$$\frac{dr}{d\lambda} = \frac{\pm\sqrt{R}}{M}, \qquad (18)$$

$$\frac{d\theta}{d\lambda} = \pm\sqrt{\Theta}, \qquad (19)$$

$$\frac{dt}{d\lambda} = T_r + T_\theta, \qquad (20)$$

$$\frac{d\phi}{d\lambda} = \Phi_r + \Phi_\theta, \qquad (21)$$

where

$$T_r = \frac{r^2 + M^2 a^2}{M\Delta}P, \qquad T_\theta = -a(aE\sin^2\theta - L_z)M \qquad (22)$$

$$\Phi_r = \frac{a}{\Delta}P - aE, \qquad \Phi_\theta = \frac{L_z}{\sin^2\theta}. \qquad (23)$$

One can see that the r and θ motions are now apparently decoupled. Next, we parametrize the orbit in terms of the (dimensionless) semilatus rectum p, the eccentricity e and a phase angle ψ via

$$r = \frac{Mp}{1 + e\cos\psi}, \qquad (24)$$

where ψ varies from 0 to 2π as r goes through a complete cycle. The two turning points of the radial motion,

$$r_a = \frac{Mp}{1 + e}, \qquad r_p = \frac{Mp}{1 - e}, \qquad (25)$$

are apoapsis and periapsis of the elliptic orbits, respectively. Moreover, the third orbital parameter is the turning point of the polar motion, θ_{tp}, which is also called the inclination angle, since this is equivalent to λ_I [43,57]. It is useful to express the constants of motion as functions of these three orbital parameters. This is implemented by solving the three equations,

$$R(r_a) = R(r_p) = \Theta(\cos\theta_{tp}) = 0. \qquad (26)$$

The asymptotic form of these constants of motion in the weak-field regime are given by

$$E = 1 + \frac{1}{2p}(e^2 - 1)(1 - qQ) + \mathcal{O}(p^{-2}), \qquad (27)$$

$$L_z = \sqrt{p}\sqrt{1 - qQ}\sin\theta_{tp} + \mathcal{O}(p^{-1/2}), \qquad (28)$$

$$C = p(1 - qQ)\cos^2\theta_{tp} + \mathcal{O}(p^0). \qquad (29)$$

Note that the terms at higher order in the $1/p$ expansion are not explicitly shown here, but they are important in the following calculations.

For bound orbits, $r(\lambda)$ and $\theta(\lambda)$ become periodic functions. Then from Eq. (18), the fundamental period for the radial motion with respect to λ is given by

$$\Lambda_r = \int_0^{\Lambda_r} d\lambda = 2\int_{r_a}^{r_p}\frac{Mdr}{\sqrt{R}} = \int_0^{2\pi}\frac{d\psi}{\sqrt{V_\psi}}, \qquad (30)$$

where we have transformed the variable of the integral from r to ψ, as the integral is easier to perform with the latter. The potential V_ψ can be obtained through R and (24).

Similarly, for the polar motion, the fundamental period is given by

$$\Lambda_\theta = 4\int_{\theta_{tp}}^{\pi/2}\frac{d\theta}{\sqrt{\Theta}} = \int_0^{2\pi}\frac{d\chi}{\sqrt{V_\chi}}, \qquad (31)$$

where we have introduced the variable χ via $\cos^2\theta = \cos^2\theta_{tp}\cos^2\chi$, such that as χ varies from 0 to 2π, θ oscillates through its full range of motion, from θ_{tp} to $\pi - \theta_{tp}$, and back [55]. Thus, the angular frequencies of the radial and the polar motion with respect to λ then become

$$\omega_r = \frac{2\pi}{\Lambda_r}, \qquad \omega_\theta = \frac{2\pi}{\Lambda_\theta}. \qquad (32)$$

For the azimuthal motion, the Eq. (21) is the sum of a function of r and a function of θ, which allows us to define the frequencies of the coordinate ϕ with respect to λ as

$$\omega_\phi = \left\langle\frac{d\phi}{d\lambda}\right\rangle_\lambda = \langle\Phi_r\rangle_\lambda + \langle\Phi_\theta\rangle_\lambda, \qquad (33)$$

where

$$\langle\Phi_r\rangle_\lambda = \frac{1}{\Lambda_r}\int\Phi_r d\lambda = \frac{1}{\Lambda_r}\int_0^{2\pi}\frac{\Phi_r}{\sqrt{V_\psi}}d\psi, \qquad (34)$$

and

$$\langle\Phi_\theta\rangle_\lambda = \frac{1}{\Lambda_\theta}\int_0^{2\pi}\frac{\Phi_\theta}{\sqrt{V_\chi}}d\chi. \qquad (35)$$

Analogously, for the motion in t, the Eq. (20) is also the sum of a function of r and a function of θ, so we can define the frequencies of the coordinate t with respect to λ as

$$\omega_t = \frac{1}{\Lambda_r}\int_0^{2\pi}\frac{T_r}{\sqrt{V_\psi}}d\psi + \frac{1}{\Lambda_\theta}\int_0^{2\pi}\frac{T_\theta}{\sqrt{V_\chi}}d\chi. \quad (36)$$

Up to now, the above fundamental frequencies were written with respect to the Mino time λ, the frequencies with respect to the distant observer time, i.e., the coordinate time t, are obtained by [53,55]

$$\Omega_r = \frac{\omega_r}{\omega_t}, \qquad \Omega_\theta = \frac{\omega_\theta}{\omega_t}, \qquad \Omega_\phi = \frac{\omega_\phi}{\omega_t}. \quad (37)$$

Explicitly, the asymptotic form of these fundamental frequencies in the weak-field regime are given by

$$\Omega_r = \frac{\sqrt{1-qQ}}{M}\left(\frac{1-e^2}{p}\right)^{3/2}$$
$$+ \frac{3\sqrt{1-qQ}(qQ-4)}{4M}\left(\frac{1-e^2}{p}\right)^{5/2}$$
$$+ \mathcal{O}(p^{-3}), \quad (38)$$

$$\Omega_\theta = \frac{\sqrt{1-qQ}}{M}\left(\frac{1-e^2}{p}\right)^{3/2} + \frac{a(1-qQ)(e^2-1)^3\sin\theta_{tp}}{Mp^3}$$
$$+ \frac{1}{M}\frac{Q(q^2Q - 3q + 2Q) - 3e^2(q^2Q^2 - 5qQ + 4))}{4(1-e^2)\sqrt{1-qQ}}$$
$$\times\left(\frac{1-e^2}{p}\right)^{5/2} + \mathcal{O}(p^{-7/2}), \quad (39)$$

$$\Omega_\phi = \frac{\sqrt{1-qQ}}{M}\left(\frac{1-e^2}{p}\right)^{3/2}$$
$$+ \frac{a(2-qQ)(1-e^2)^{3/2} + a(1-qQ)(e^2-1)^3\sin\theta_{tp}}{Mp^3}$$
$$+ \frac{-Q(-3q + 2Q + q^2Q) + 3e^2(4 - 5qQ + q^2Q^2)}{4M(1-e^2)\sqrt{1-qQ}}$$
$$\times\left(\frac{1-e^2}{p}\right)^{5/2} + \mathcal{O}(p^{-7/2}). \quad (40)$$

Therefore, we obtain the perihelion precession frequency and the orbital plane precession frequency at the leading order of the $1/p$ expansion,

$$\dot{\tilde{\gamma}} = \frac{1}{M}\frac{6 - 6Qq - Q^2 + q^2Q^2}{2(1-e^2)\sqrt{1-qQ}}\left(\frac{1-e^2}{p}\right)^{5/2}, \quad (41)$$

$$\dot{\alpha} = \frac{a(2-qQ)(1-e^2)^{3/2}}{Mp^3}. \quad (42)$$

Comparing with the uncharged equations, the modification due to the charges in the system can be summarized as the electric force between the CO and the KN BH in the form qQ and the deformation of the metric from the charge of the KN BH in the form Q^2. As we will see in the next

subsection, the other contribution of the charges to the waveforms stems from the dipole electromagnetic radiation in the form $(Q-q)^2$.

C. Fluxes

Besides the fundamental frequencies, the other piece of the AK waveform is the change rates of the eccentricity e and the radial orbital frequency ν with respect to the coordinate time, which are related to the energy flux and the angular momentum flux due to the gravitational radiation and electromagnetic radiation.

For the gravitational radiation, the standard quadrupole formulas of the energy flux and the angular momentum flux were already derived by Peters and Mathews [49,50],

$$\left\langle\frac{dE}{dt}\right\rangle = \frac{1}{5\mu}\left\langle\frac{d^3Q_{ij}}{dt^3}\frac{d^3Q^{ij}}{dt^3} - \frac{1}{3}\frac{d^3Q_i^i}{dt^3}\frac{d^3Q_j^j}{dt^3}\right\rangle, \quad (43)$$

and

$$\left\langle\frac{dL_i}{dt}\right\rangle = \frac{2}{5\mu M}\epsilon_{ijk}\left\langle\frac{d^2Q_{jm}}{dt^2}\frac{d^3Q^{km}}{dt^3}\right\rangle, \quad (44)$$

where μ is the reduced mass $\mu = mM/(m+M) \simeq m$, E and L_i are the dimensionless energy and angular momentum appeared in the equations of motion of the charged CO. Q_{ij} is the familiar quadrupole moment tensor of mass (also called the inertia tensor),

$$Q_{ij} = \mu x^i x^j, \quad (45)$$

where x^i is the relative position vector between the charged CO and the charged central BH, and in the weak-field regime, one has $x^i = (r\cos\phi\sin\theta, r\sin\phi\sin\theta, r\cos\phi)$. In addition, the angle brackets mean the average over one cyclic motion in r, which via (24), can be turned into the integral for ψ,

$$\left\langle\frac{dE}{dt}\right\rangle = \frac{1}{T}\int_0^{2\pi}\frac{dE}{dt}\frac{d\psi}{\dot\psi}, \qquad T = \int_0^{2\pi}\frac{d\psi}{\dot\psi}. \quad (46)$$

In the following, without ambiguity, we will just use dE/dt and dL_z/dt to denote the averaged ones. Then from above formulas and the equations of motion of the CO, we obtain the energy flux and angular momentum flux loss of the charged particle due to the gravitational radiation,

$$\frac{dE}{dt} = -\frac{32\eta}{5Mp^5}(1-qQ)^3(1-e^2)^{3/2}\left(1 + \frac{73}{24}e^2 + \frac{37}{96}e^4\right), \quad (47)$$

$$\frac{dL_z}{dt} = -\frac{32\eta\sin\theta_{tp}}{5Mp^{7/2}}(1-qQ)^{5/2}(1-e^2)^{3/2}\left(1 + \frac{7}{8}e^2\right), \quad (48)$$

where the assumption that we have made is same to [35] in which θ_{tp} is constant at leading order in the $1/p$ expansion.

To simplify the expressions, we have introduced the symmetric mass ratio,

$$\eta \equiv \frac{mM}{(m+M)^2} \simeq \frac{m}{M}. \tag{49}$$

In terms of the relation between p and the radial orbital frequency at leading order,

$$p = \frac{(1-e^2)(1-qQ)^{1/3}}{(2\pi M\nu)^{2/3}}, \tag{50}$$

the above two equations can be written as

$$\frac{dE}{dt} = -\frac{32\eta}{5M}(2\pi M\nu)^{10/3}(1-qQ)^{4/3}(1-e^2)^{-7/2}$$
$$\times \left(1 + \frac{73}{24}e^2 + \frac{37}{96}e^4\right), \tag{51}$$

$$\frac{dL_z}{dt} = -\frac{32\eta \sin\theta_{tp}}{5M}(2\pi M\nu)^{7/3}(1-qQ)^{4/3}(1-e^2)^{-2}$$
$$\times \left(1 + \frac{7}{8}e^2\right). \tag{52}$$

On the other hand, from the asymptotic form of the energy and angular momentum in the weak-field regime (27) and (28), we can obtain their change rates with respect to distant observer time,

$$\frac{dE}{dt} = -\frac{(2\pi M)^{2/3}(1-qQ)^{2/3}}{3\nu^{1/3}}\frac{d\nu}{dt}, \tag{53}$$

$$\frac{dL_z}{dt} = -\frac{(1-qQ)^{2/3}\sin\theta_{tp}}{3(2\pi M\nu)^{1/3}\sqrt{1-e^2}\nu}$$
$$\times \left(3e\nu\frac{de}{dt} + (1-e^2)\frac{d\nu}{dt}\right). \tag{54}$$

We should also take the orbit decay due to the electromagnetic radiation into account. The formulas of the energy and angular emission rates for the dipole electromagnetic radiation [58] are given by [59] and also [60–63],

$$m\frac{dE_{EM}}{dt} = \frac{2}{3}\mu^2(Q-q)^2\left\langle\frac{d^2x^i}{dt^2}\frac{d^2x_i}{dt^2}\right\rangle, \tag{55}$$

and

$$mM\frac{dL_z^{EM}}{dt} = \frac{2}{3}\mu^2(Q-q)^2\epsilon^{jkl}\left\langle\frac{dx_k}{dt}\frac{d^2x_l}{dt^2}\right\rangle, \tag{56}$$

where as before the angle brackets denote the average over one period in r motion, and $j = z$. It should be noted that the above mentioned E^{EM} and L_z^{EM} are set to be dimensionless, their relation with the original ones are the same as (12). Then for a charged particle orbiting a KN BH, the energy flux, and angular momentum flux loss due to the electromagnetic radiation at the leading order in $1/p$ expansion are given by

$$\frac{dE_{EM}}{dt} = -\frac{(2+e^2)\eta^2}{3(1-e^2)^{5/2}}(2\pi mM\nu)^{8/3}(Q-q)^2$$
$$\times (1-qQ)^{2/3}, \tag{57}$$

$$\frac{dL_z^{EM}}{dt} = -\frac{2m\sin\theta_{tp}}{3M^3(1-e^2)}(2\pi M\nu)^{5/3}(Q-q)^2$$
$$\times (1-qQ)^{2/3}. \tag{58}$$

Combining the Eqs. (51)–(58), we have the evolution equations of orbital eccentricity e and ν due to the gravitational and electromagnetic radiation,

$$\frac{d\nu}{dt} = \frac{96}{10\pi}\frac{\eta}{M^2}(2\pi M\nu)^{11/3}(1-qQ)^{2/3}(1-e^2)^{-7/2}$$
$$\times \left(1 + \frac{73}{24}e^2 + \frac{37}{96}e^4\right)$$
$$+ \frac{\eta(2+e^2)(Q-q)^2(2\pi M\nu)^3(1-e^2)^{-5/2}}{2\pi M^2}, \tag{59}$$

$$\frac{de}{dt} = -\frac{e\eta}{15M}(2\pi M\nu)^{8/3}(1-qQ)^{2/3}$$
$$\times (1-e^2)^{-5/2}(304+121e^2)$$
$$- \frac{e\eta}{M}(Q-q)^2(2\pi M\nu)^2(1-e^2)^{-3/2}. \tag{60}$$

From the right-hand sides of these equations, we find that the contribution from the dipole electromagnetic radiation is lower than that from the gravitational radiation by a factor of $(2\pi M\nu)^{2/3}$, which for a Keplerian orbit corresponds to v^2, where v is the orbital velocity of the CO. This means that the correction due to the dipole electromagnetic radiation appears at -1 PN order in the waveforms and becomes prominent at the early stage of the inspiral of the CO where v is small. This is verified by numerical relativity simulations of the coalescence of the charged binary BHs with comparable masses [16], where it was found that the greatest difference between charged and uncharged BHs arises in the earlier inspiral. In this case, despite the fact that the AK model is not accurate enough to produce EMRI template waveforms in the strong field region, the behavior of the electric charges may well be captured by this model.

In terms of the radial frequency ν, the other two Eqs. (41) and (42) are expressed as

$$\frac{d\tilde{\gamma}}{dt} = \frac{(6-6Qq-Q^2+q^2Q^2)}{(1-qQ)^{4/3}(1-e^2)}\pi\nu(2\pi M\nu)^{2/3}, \tag{61}$$

$$\frac{d\alpha}{dt} = \frac{4a(2-qQ)\pi^2M\nu^2}{(1-e^2)^{3/2}(1-qQ)}. \tag{62}$$

From these four evolution equations, we can see that the equations keep invariant under the operation $q \to -q$ and $Q \to -Q$, which means we cannot simultaneously determine the sign of q and Q. Hereafter, without loss of generality, we will always assume that the charge of the MBH is positive and let the sign of the charge of the orbiting particle to be free. For gravitational waveform generated by two charged compact objects moving on a Keplerian orbit in a plane, the charges appear only in the form $(Q-q)^2$ and qQ, which hinders the unique determination of the two charges. However, the relativistic effects considered in the AK waveform breaks the degeneracy between these two terms. As a consequence, once the sign of Q is provided, we can not only identify the value of Q but also uniquely discern both the magnitude and the sign of q. Even the dipole electromagnetic radiation disappears when $Q = q$, this conclusion still works.

Up to now, we have obtained the leading order evolution equations for the relevant orbital parameters when both the CO and central BH are charged. In analogy with the construction of EMRI waveforms in alternative theories of gravity, e.g., [33], we combine these leading order corrected equations with those higher-order PN equations in the original AK model. Then the complete orbital evolution equations are given by [64]

$$\dot{\Phi} = 2\pi\nu,$$

$$
\begin{aligned}
\dot{\nu} &= \frac{48}{5\pi}\frac{\eta}{M^2}X^{11/3}Y^{-9/2}\left\{(1-qQ)^{2/3}Y\left(1+\frac{73}{24}e^2+\frac{37}{96}e^4\right)\right. \\
&\quad + X^{2/3}\left[\frac{1273}{336}-\frac{2561}{336}e^2-\frac{3885}{128}e^4-\frac{13147}{5376}e^6\right] \\
&\quad \left.- Xa\cos\lambda Y^{-1/2}\left[\frac{73}{12}+\frac{1211}{24}e^2+\frac{3143}{96}e^4+\frac{65}{64}e^6\right]\right\} \\
&\quad + \frac{\eta(Q-q)^2}{2\pi M^2}X^3(2+e^2)Y^{-5/2},
\end{aligned}
$$

$$
\begin{aligned}
\dot{e} &= -\frac{e\eta}{15M}Y^{-7/2}X^{8/3}\left[\left((1-qQ)^{2/3}+12X^{2/3}\right)\right. \\
&\quad \times (304+121e^2)Y \\
&\quad \left.- \frac{1}{56}X^{2/3}(133640+108984e^2+25211e^4)\right] \\
&\quad + e\frac{\eta}{M}a\cos\lambda X^{11/3}Y^{-4}\left(\frac{1364}{5}+\frac{5032}{15}e^2+\frac{263}{10}e^4\right) \\
&\quad - e\frac{\eta}{M}(Q-q)^2X^2Y^{-3/2},
\end{aligned}
$$

$$
\begin{aligned}
\dot{\tilde{\gamma}} &= \pi\nu X^{2/3}Y^{-1}\left[(6-6qQ-Q^2+q^2Q^2)(1-qQ)^{-4/3}\right. \\
&\quad \left.+ \frac{3}{2}X^{2/3}Y^{-1}(26-15e^2)\right] - 12\pi\nu a\cos\lambda XY^{-3/2},
\end{aligned}
$$

$$\dot{\alpha} = 4aM(\pi\nu)^2Y^{-3/2}(2-qQ)/(1-qQ), \qquad (63)$$

where dot denotes the derivative with respect to time and to avoid redundant expression, we have defined $Y = 1 - e^2$, $X = 2\pi M\nu$. The equation for $\dot{\nu}$ and $\dot{e}$ are given accurately through 3.5 PN order, the equations for $\dot{\tilde{\gamma}}$ and $\dot{\alpha}$ are accurate through 2 PN order.

We would like to give a brief review of how do above evolving orbital parameters enter the AK EMRI waveforms. The general GW strain field at the detector is written as

$$h_{ij}(t) = A^+(t)H_{ij}^+(t) + A^\times(t)H_{ij}^\times(t), \qquad (64)$$

where H_{ij}^+ and $H_{ij}^\times$ are the two polarization basis tensors constructed with the unit vector pointing from the detector to the source $\hat{n}$ and the unit vector along the CO's orbital angular momentum $\hat{L}$,

$$H_{ij}^+(t) = \hat{p}_i\hat{p}_j - \hat{q}_i\hat{q}_j, \qquad H_{ij}^\times(t) = \hat{p}_i\hat{q}_j + \hat{q}_i\hat{p}_j, \qquad (65)$$

with

$$\hat{p} = \frac{\hat{n}\times\hat{L}}{|\hat{n}\times\hat{L}|}, \qquad \hat{q} = \hat{p}\times\hat{n}, \qquad (66)$$

and A^+ and $A^\times$ are the amplitudes of the two polarizations. The amplitudes of the two polarizations can be further written in terms of the Peters-Mathews harmonic decomposition as

$$
\begin{aligned}
A^+ &\equiv \sum_n A_n^+ \\
&= \sum_n -[1+(\hat{L}\cdot\hat{n})^2][a_n\cos 2\gamma - b_n\sin 2\gamma] \\
&\quad + c_n[1-(\hat{L}\cdot\hat{n})^2], \qquad (67)
\end{aligned}
$$

$$
\begin{aligned}
A^\times &\equiv \sum_n A_n^\times \\
&= \sum_n 2(\hat{L}\cdot\hat{n})[b_n\cos 2\gamma + a_n\sin 2\gamma], \qquad (68)
\end{aligned}
$$

where (a_n, b_n, c_n) come from decomposition of the second time derivative of the inertia tensor Q^{ij} into n—harmonics of the radial orbital frequency ν and are functions of ν and e [49]. Moreover, γ is an azimuthal angle measuring the direction of pericenter with respect to the orthogonal projection of $\hat{n}$ onto the orbital plane, which further depends on $\tilde{\gamma}$ and α.

Since the equilateral triangle detectors such as TQ can be used to construct two independent Michelson interferometers, the signal responded by such two interferometers can be written as

$$h_{I,II} = \frac{\sqrt{3}}{2}(F_{I,II}^+h^+ + F_{I,II}^\times h^\times), \qquad (69)$$

where the antenna pattern function $F_{I,II}^{+,\times}$ of the detector depend on the orbits of satellites [65]. For TQ, the detailed information of the respond function for EMRI signal can be found in [32].

At the final stage of EMRI, when the CO passed the boundary of stable orbits, it will plunge into the MBH directly in a short time. So we need to introduce a cutoff frequency to the waveform. When the CO is moving in the equatorial plane of the central BH, the cutoff is usually taken to be the last stable orbit (LSO). Here, for simplicity, we take the innermost stable circular orbit (ISCO) as the cutoff in our waveform. The radius of the ISCO results from the equations $R(r) = R'(r) = R''(r) = 0$. Although these equations can be solved analytically with *Mathematica*, the expression of the solution is very lengthy so we shall not show it here. Instead, the effects of the MBH charge Q and CO charge q on the ISCO radius can be demonstrated clearly in a graphical manner. Note that in this work, we only consider the prograde orbits of the CO, since most of the detected events have prograde orbits [32].

As shown in Fig. 1, r_{ISCO} changes gradually with the MBH charge Q (left panel) and CO charge q (right panel). This indicates that the CO gets a chance to orbit more circles in the vicinity of the KN BH, and the charged EMRI system radiates higher frequency GW signal than the neutral system. The effect of the CO charge on r_{ISCO} is
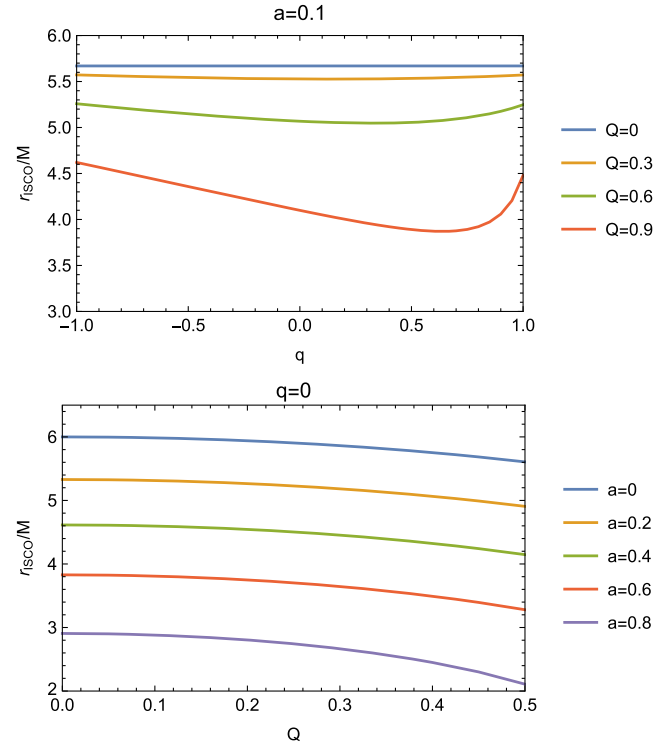

FIG. 1. The influence on the radius of ISCO by the charge of CO and MBH, and the spin of MBH. Above: The r_{ISCO} as a function of q for different Q. Below: The r_{ISCO} as a function of Q for different a.

more complicated. In this case, r_{ISCO} no longer depends on q monotonically. Nevertheless, the turning point at which the monotonicity of q changes increase with Q.

III. METHOD OF GW ANALYSIS

In this section, we present some recipes for the assessing of the impacts the charge parameters q and Q on the EMRI waveforms and the constraint on them with LISA and TianQin observations of EMRIs.

To assess the effects the charges of the MBH and CO on the EMRI waveforms, it is convenient to define the overlap $\mathcal{O}$ between two sets of waveforms $h_a(t)$ and $h_b(t)$,

$$\mathcal{O}(h_a|h_b) = \frac{\langle h_a|h_b \rangle}{\sqrt{\langle h_a|h_a \rangle \langle h_b|h_b \rangle}}, \qquad (70)$$

where the inner product $\langle h_a|h_b \rangle$ is defined by

$$\langle h_a|h_b \rangle = 2 \int_0^\infty df \frac{h_a^*(f)h_b(f) + h_a(f)h_b^*(f)}{S_n(f)}. \qquad (71)$$

Here, $h_a(f)$ is the Fourier transform of the time domain waveform $h_a(t)$, $*$ denotes complex conjugate and $S_n(f)$ is noise power spectral density of space-borne GW detectors, such as LISA [29] and TianQin (TQ) [28]. Hence, we get the mismatch $\mathcal{M}$ for two different waveforms,

$$\mathcal{M} \equiv 1 - \mathcal{O}(h_a|h_b). \qquad (72)$$

Obviously, if the two waveforms are identical, the overlap between them equates to unity and so their mismatch is zero. For a signal with signal-to-noise ratio (SNR) ρ, the mismatch of two different waveforms has to be larger than $\mathcal{D}/2\rho^2$ for a detector to distinguish them [66,67], where $\mathcal{D} = 9$ denotes the number of the intrinsic parameters of the EMRI system. The intrinsic parameters describe the system without reference to the location or orientation of the observer [68]. For example, the SNR threshold for EMRI that can be detected is usually chosen to be 20 [30]. Then the mismatch of two waveforms larger than 0.01125 can be resolved for a EMRI event, which has just reached the threshold of detection.

A. Fisher informational matrix

To quantify the capability of space-borne GW detectors to constrain the MBH and CO charges, we use the fisher informational matrix (FIM) method [69] to obtain the lowest-order expansion of the posteriors (valid in the high SNR limit), which can be more accurately estimated through a full Bayesian parameter estimation analysis.

The FIM is defined by

$$\Gamma_{ab} = \left(\frac{\partial h}{\partial \lambda_a} \bigg| \frac{\partial h}{\partial \lambda_b} \right), \qquad (73)$$

where λ_a, $a = 1, 2, \ldots$, are the parameters appearing in the waveform (13) and the inner product $(|)$ is defined by Eq. (71). When the SNR of the GW signal is large, the variance-covariance matrix can be obtained as the inverse of the FIM,

$$\Sigma_{ab} \equiv \langle \Delta\lambda_a \Delta\lambda_b \rangle = (\Gamma^{-1})_{ab}. \tag{74}$$

From the variance-covariance matrix, the uncertainty σ_a of the ath parameter λ_a can be obtained as

$$\delta\lambda_a = \Sigma_{aa}^{1/2}. \tag{75}$$

Note that the applicability of the FIM method requires the linear signal approximation to be valid [69], so strictly speaking, we should verify this point. By following the procedure in [69] and for LISA, we calculate the cumulative distribution function for mismatch ratio r, which characterizes the difference between the actual value of likelihoods and the linear signal approximation. The criterion is when $|\log r| < 0.1$ over 90% of the 1σ surface for a given SNR, we can say the FIM method is valid. In Fig. 2, we show the cumulative distribution function (CDF) for logarithm of r at SNR $\rho = 20$, with $Q = q = 0$, $Q = 0.1, q = -0.4$ and $Q = 0.2, q = -0.1$. We can see that for most of the random points at the 1σ surface, the derived value of likelihood using FIM slightly deviations from the exact likelihood, which means the parameter estimation for charged EMRI system with FIM method is basically valid.
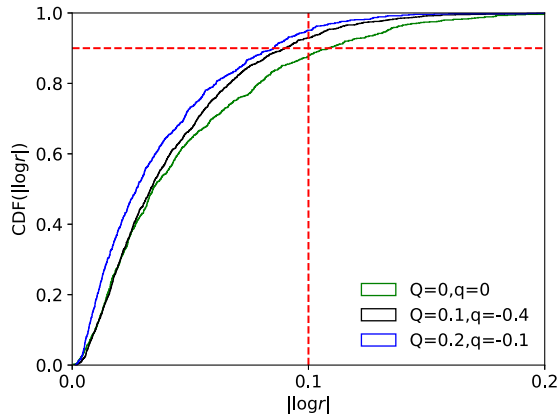

FIG. 2. Cumulative distribution function of logarithm of mismatch ratio $\log(r)$ for different charges, assuming the SNR $\rho = 20$, is plotted. The horizontal and vertical dashed line represents 90% point of CDF of $|\log(r)|$ and $|\log(r)| = 0.1$, respectively. The FIM is valid when the curve surpassed these dashed lines. The other parameters take values as those in Sec. IV A.

IV. RESULTS

A. Waveforms and mismatch

By solving above orbital evolution equations (63) numerically, we can plot the charged AK waveforms in the time domain. In Fig. 3, we show the comparison of the charged AK waveforms with the neutral ones in various cases. Since we focus on the charge parameters in the waveform, we let the other parameters in (13) to be fixed as follows: $t_0 = 1$ years, $D = 1$ Gpc, $m = 10 M_\odot$, $M = 10^6 M_\odot$, $e = 0.1$, $\lambda = \pi/3$, $\tilde{\gamma}_0 = 5\pi/6$, $\alpha_0 = 4\pi/5$, $\theta_S = \pi/5$, $\phi_S = \pi/4$, $\theta_K = 2\pi/3$, $\phi_K = 3\pi/4$, $\Phi_0 = \pi/3$, and $\nu_0 = 1$ mHz. Note that for comparison, when plotting the waveforms, we set the initial radial orbital frequency of the charged and neutral cases to be the same, so here t_0 denotes the duration time of the waveforms.

From Fig. 3, we can see that the AK waveforms are significantly affected by the charges of the system. In this case, the initial radial orbital frequencies of two EMRI systems are set to be the same as each other, so the waveforms at $t = 0$ should also be identical, and the effects of charges on waveform will grow with the increasing time. Particularly, when both members of the EMRI are charged, the dephasing occurs very quickly in the first 30000 seconds at the beginning as showed by the panel on the left of the bottom. If only the CO is charged, and the MBH is neutral, although the waveform is almost the same for the case that both objects are neutral, by a long accumulation of time, the dephasing is still visible from the top panel on the right. For the case that only the MBH is charged, and the CO is neutral, the dephasing is not very significant even after 1 year as showed by the right panel in the middle, but the mismatch also exceed the threshold as plotted in Fig. 4. In fact, if the MBH carries the same amount of charges as the CO, the dephasing of the former would be more prominent, as we will see below.

To assess the effect of charge on EMRI waveform quantitatively, we calculate the mismatch for neutral waveform and the charged waveform. As shown in Fig. 4, the mismatch is plotted as the function of observation time for TQ, where the initial radial orbital frequencies for the two waveforms are set as 1 mHz and the SNR of the signal is set to be 20. According to Fig. 4, the mismatch can exceed the threshold value $\mathcal{M}_{\min} = 0.01125$ even though the charges of EMRI system are small to 10^{-3}. From the upper two panels of Fig. 4 where only one member carries charge, one can see that TQ can distinguish the modified waveform with charge $Q, q \approx 10^{-3}$ in three months. When both the members of the EMRI carry charge $Q = 10^{-3}, q = 3 \times 10^{-3}$ as shown in the bottom panel, the effects of charges on AK waveform would be recognized within two months. However, if both of the two objects carries the charges less than the level of 10^{-4}, the mismatch will not exceed the threshold, and thus, we cannot distinguish whether the CO and the MBH have charges or not. Furthermore, we can see that the MBH charge Q yields slightly different influence
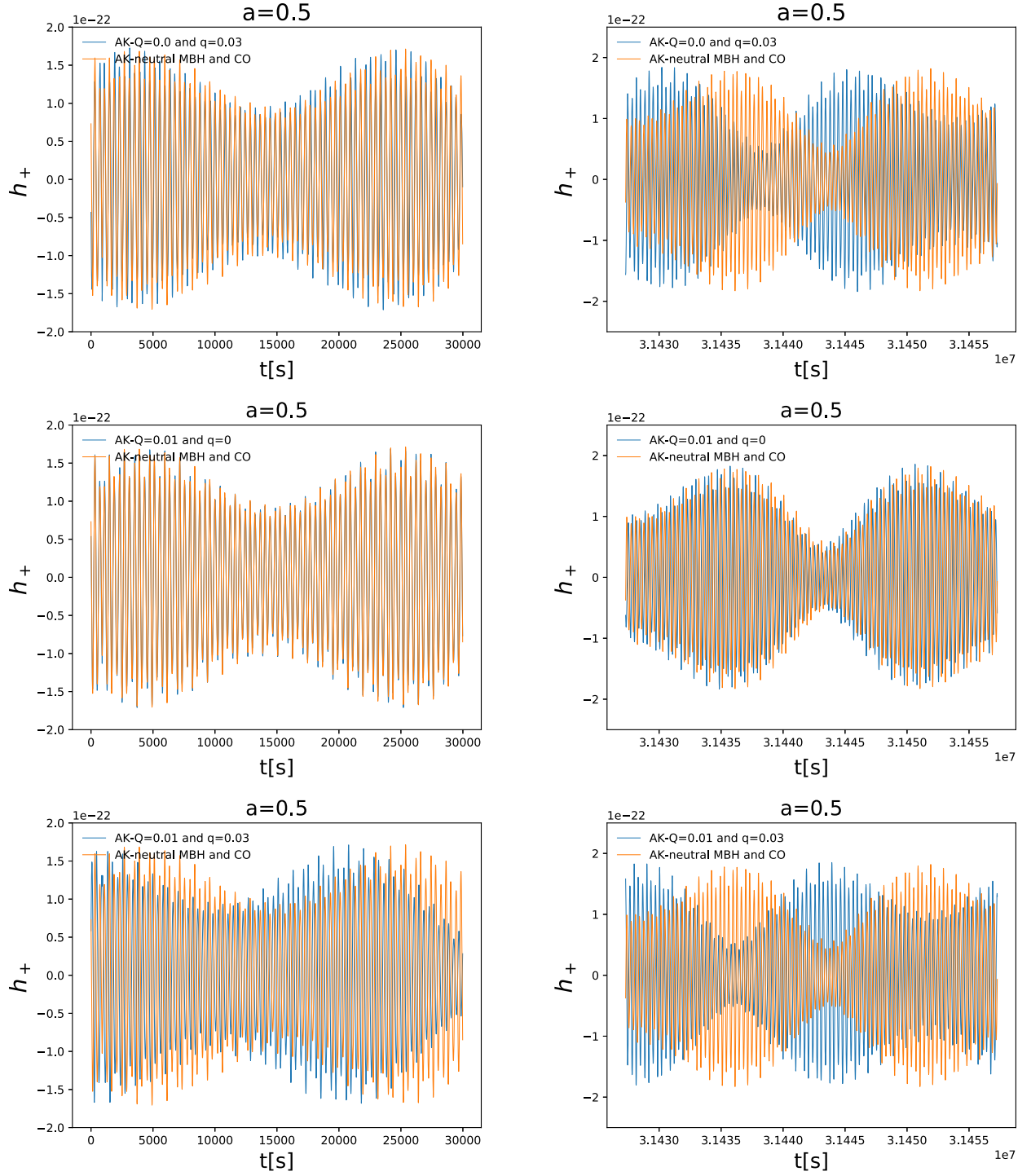
FIG. 3. Comparison among plus polarization h_+ of AK waveforms from charged EMRI in the case of spin $a = 0.5$ for several examples, where the initial frequency is set as $\nu_0 = 1$ mHz. Top panels: the CO is charged with $q = 0.03$ and the central BH is neutral with $Q = 0$. Middle panels: the central BH is charged with $Q = 0.01$ and the CO is neutral with $q = 0$. Bottom panels: both the MBH and the CO are charged with $Q = 0.01$ and charged CO with $q = 0.03$. The other parameters are set as Sec. IV A. The length of the waveform is 1 year, and the left panels represent the waveform for the first 30000 seconds, while the right panels for the last 30000 seconds.

on the AK waveforms than that of the CO charge q, it is because that the effects of MBH charge and CO charge on the waveform are not equal, the former can also affect the waveform through its deformation on the metric.

To assess the effects of charges on the waveform more clearly, we plot the mismatch as a function of both Q and q for LISA and TQ respectively in Fig. 5. As it is shown, the black dotted line represents the contour of mismatch
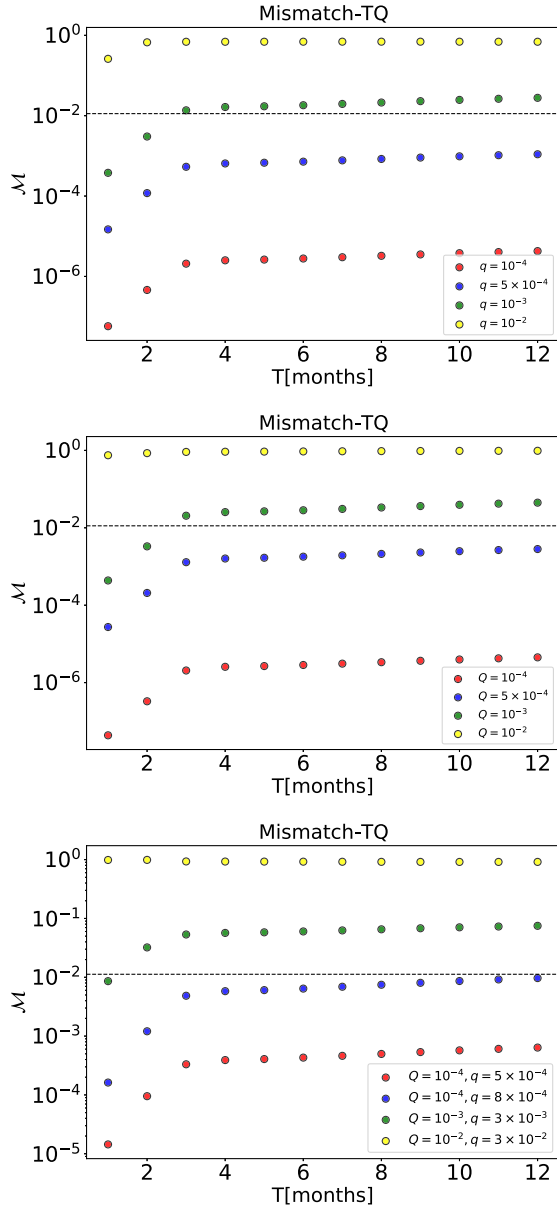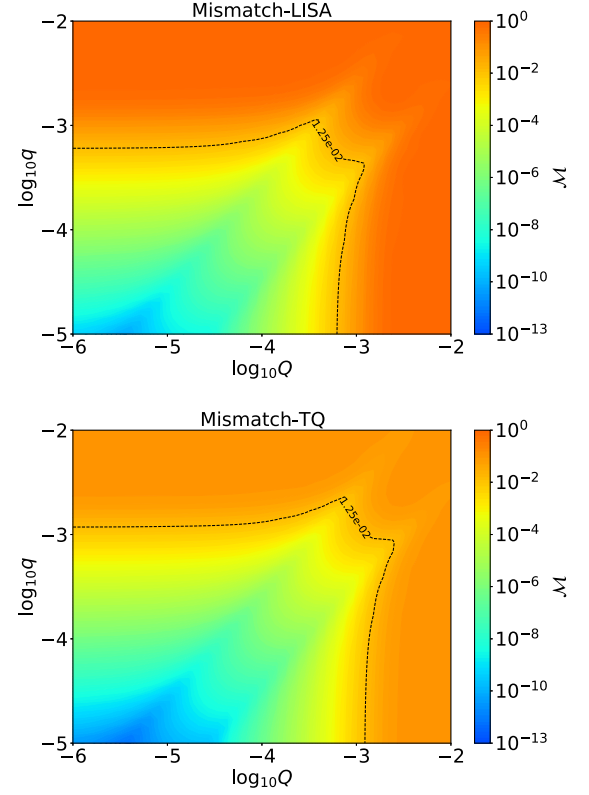
FIG. 5. The contour plot of the mismatch $\mathcal{M}$ as a function of $\log_{10} Q$ and $\log_{10} q$ with respect to LISA (top panel) and TQ (bottom panel), respectively. The black dashed line denotes to the threshold value for SNR = 20, where the source parameters are set as $M = 10^6 M_\odot$, $a = 0.4$, and the other parameters keep same with the previous configurations in Fig. 3.

FIG. 4. The mismatch $\mathcal{M}$ as a function of observation time for TianQin is plotted, the dashed lines represent the threshold for SNR = 20. The source parameters are set as $M = 10^6 M_\odot$, $a = 0.5$, the charge Q of MBH is 0 in the top panel and the charge of CO is 0 in the middle panel, the other parameters keep same with the previous configurations in Fig. 3.

equal to the threshold $\mathcal{M} = 0.01125$, it indicates that the space-borne GW detectors can distinguish whether the objects in an EMRI is charged if the system is located beyond this curve. The behavior of mismatch contour plots for LISA and TQ is almost the same, the threshold values for charges are about $Q \approx 10^{-3}$ and $q \approx 10^{-3}$, respectively, and the value for LISA is lower than TQ, since it will have better performance in lower frequency band.

To study whether the presence of charges will cause some bias on the parameter estimation even if the mismatch

does not exceed the threshold, we calculate the mismatch between the waveforms from a charged EMRI and from a neutral EMRI keeping all the parameters the same as the previous one except the mass of the MBH. The deviation of M is noted as δM, we keep this parameter M changing
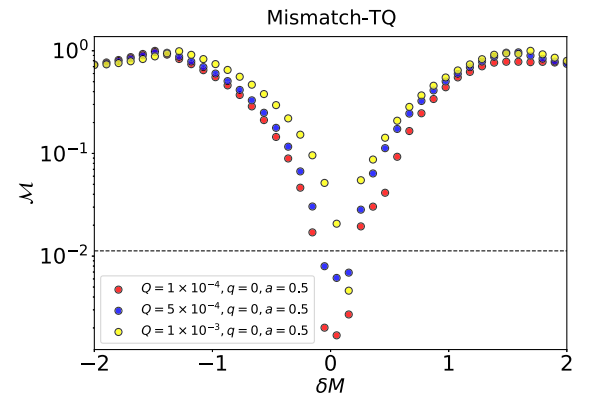

FIG. 6. The mismatch $\mathcal{M}$ as a function of mass variation δM of MBH for TianQin. The source parameters are set as $M = (10^6 + \delta M) M_\odot$, $a = 0.5$, and $q = 0$ the other parameters keep same with the previous configurations in Fig. 3.

TABLE I. ΔQ for different mass M and spin a of the MBH is listed. The plain and bold values correspond to the observation of LISA and TQ, respectively. Two charge parameters q and Q both are set as zero. The other parameters keep same with the previous configurations in Fig. 3.

	MBH mass $\log_{10}(M/M_\odot)$				
a	5.0	5.5	6.0	6.5	7.0
0.01	4.5×10^{-3}	7.8×10^{-3}	2.1×10^{-1}	$\cdots$	$\cdots$
	$\mathbf{4.7 \times 10^{-3}}$	$\mathbf{9.1 \times 10^{-2}}$	$\mathbf{3.2 \times 10^{-1}}$	$\cdots$	$\cdots$
0.15	3.2×10^{-3}	6.8×10^{-3}	4.8×10^{-2}	$\cdots$	$\cdots$
	$\mathbf{4.2 \times 10^{-3}}$	$\mathbf{2.4 \times 10^{-2}}$	$\mathbf{1.2 \times 10^{-1}}$	$\cdots$	$\cdots$
0.25	2.5×10^{-3}	4.6×10^{-3}	4.7×10^{-2}	2.4×10^{-1}	$\cdots$
	$\mathbf{3.9 \times 10^{-3}}$	$\mathbf{7.8 \times 10^{-3}}$	$\mathbf{8.8 \times 10^{-2}}$	$\mathbf{7.7 \times 10^{-1}}$	$\cdots$
0.35	2.3×10^{-3}	4.3×10^{-3}	2.9×10^{-2}	1.7×10^{-1}	$\cdots$
	$\mathbf{3.8 \times 10^{-3}}$	$\mathbf{6.2 \times 10^{-3}}$	$\mathbf{7.2 \times 10^{-2}}$	$\mathbf{3.4 \times 10^{-1}}$	$\cdots$
0.45	2.2×10^{-3}	3.1×10^{-3}	1.9×10^{-2}	6.8×10^{-2}	$\cdots$
	$\mathbf{3.6 \times 10^{-3}}$	$\mathbf{4.3 \times 10^{-3}}$	$\mathbf{6.1 \times 10^{-2}}$	$\mathbf{2.1 \times 10^{-1}}$	$\cdots$
0.55	2.1×10^{-3}	2.6×10^{-3}	1.4×10^{-2}	5.3×10^{-2}	$\cdots$
	$\mathbf{3.4 \times 10^{-3}}$	$\mathbf{2.8 \times 10^{-3}}$	$\mathbf{2.5 \times 10^{-2}}$	$\mathbf{1.4 \times 10^{-1}}$	$\cdots$
0.65	1.8×10^{-3}	2.3×10^{-3}	9.5×10^{-3}	4.3×10^{-2}	9.4×10^{-1}
	$\mathbf{3.2 \times 10^{-3}}$	$\mathbf{2.5 \times 10^{-3}}$	$\mathbf{1.8 \times 10^{-2}}$	$\mathbf{9.2 \times 10^{-2}}$	$\mathbf{8.6 \times 10^{-1}}$
0.75	1.5×10^{-3}	2.3×10^{-3}	5.8×10^{-3}	4.3×10^{-1}	3.7×10^{-1}
	$\mathbf{1.7 \times 10^{-3}}$	$\mathbf{2.4 \times 10^{-2}}$	$\mathbf{6.1 \times 10^{-3}}$	$\mathbf{3.4 \times 10^{-2}}$	$\mathbf{4.5 \times 10^{-2}}$
0.85	9.7×10^{-4}	1.6×10^{-3}	1.5×10^{-3}	1.4×10^{-2}	1.1×10^{-1}
	$\mathbf{1.6 \times 10^{-3}}$	$\mathbf{1.8 \times 10^{-3}}$	$\mathbf{3.7 \times 10^{-3}}$	$\mathbf{7.7 \times 10^{-3}}$	$\mathbf{3.3 \times 10^{-2}}$
0.95	1.6×10^{-4}	8.8×10^{-4}	1.3×10^{-3}	6.5×10^{-3}	5.1×10^{-2}
	$\mathbf{3.5 \times 10^{-4}}$	$\mathbf{1.3 \times 10^{-3}}$	$\mathbf{2.7 \times 10^{-3}}$	$\mathbf{2.3 \times 10^{-3}}$	$\mathbf{2.1 \times 10^{-2}}$

TABLE II. Δq for different mass M and spin a of the MBH is listed. The plain and bold values correspond to the observation of LISA and TQ, respectively. Two charge parameters q and Q both are set as zero. The other parameters keep same with the previous configurations in Fig. 3.

	MBH mass $\log_{10}(M/M_\odot)$				
a	5.0	5.5	6.0	6.5	7.0
0.01	1.3×10^{-3}	1.4×10^{-3}	4.6×10^{-2}	8.3×10^{-1}	$\cdots$
	$\mathbf{1.9 \times 10^{-3}}$	$\mathbf{7.1 \times 10^{-2}}$	$\mathbf{1.7 \times 10^{-1}}$	$\mathbf{8.8 \times 10^{-1}}$	$\cdots$
0.15	1.1×10^{-3}	1.3×10^{-3}	9.4×10^{-3}	5.1×10^{-1}	$\cdots$
	$\mathbf{8.2 \times 10^{-3}}$	$\mathbf{1.7 \times 10^{-2}}$	$\mathbf{1.1 \times 10^{-1}}$	$\mathbf{7.5 \times 10^{-1}}$	$\cdots$
0.25	7.4×10^{-4}	8.4×10^{-4}	9.2×10^{-3}	3.7×10^{-1}	$\cdots$
	$\mathbf{6.2 \times 10^{-3}}$	$\mathbf{5.6 \times 10^{-3}}$	$\mathbf{6.4 \times 10^{-2}}$	$\mathbf{4.7 \times 10^{-1}}$	$\cdots$
0.35	5.6×10^{-4}	7.9×10^{-4}	5.8×10^{-3}	2.5×10^{-1}	$\cdots$
	$\mathbf{5.6 \times 10^{-3}}$	$\mathbf{4.9 \times 10^{-3}}$	$\mathbf{5.2 \times 10^{-2}}$	$\mathbf{3.4 \times 10^{-1}}$	$\cdots$
0.45	5.1×10^{-4}	6.5×10^{-4}	3.6×10^{-3}	1.7×10^{-1}	$\cdots$
	$\mathbf{3.5 \times 10^{-3}}$	$\mathbf{4.8 \times 10^{-3}}$	$\mathbf{4.6 \times 10^{-2}}$	$\mathbf{2.5 \times 10^{-1}}$	$\cdots$
0.55	4.7×10^{-4}	6.3×10^{-4}	2.6×10^{-3}	1.2×10^{-1}	$\cdots$
	$\mathbf{2.6 \times 10^{-3}}$	$\mathbf{1.1 \times 10^{-3}}$	$\mathbf{2.5 \times 10^{-2}}$	$\mathbf{1.4 \times 10^{-1}}$	$\cdots$
0.65	3.5×10^{-4}	5.8×10^{-4}	1.8×10^{-3}	6.2×10^{-2}	7.9×10^{-1}
	$\mathbf{1.9 \times 10^{-3}}$	$\mathbf{6.2 \times 10^{-4}}$	$\mathbf{1.7 \times 10^{-2}}$	$\mathbf{6.8 \times 10^{-2}}$	$\mathbf{5.4 \times 10^{-1}}$
0.75	1.6×10^{-4}	4.2×10^{-4}	1.1×10^{-3}	2.8×10^{-2}	5.1×10^{-1}
	$\mathbf{2.4 \times 10^{-4}}$	$\mathbf{4.4 \times 10^{-4}}$	$\mathbf{1.2 \times 10^{-2}}$	$\mathbf{1.8 \times 10^{-2}}$	$\mathbf{2.2 \times 10^{-1}}$
0.85	1.1×10^{-4}	3.5×10^{-4}	4.7×10^{-4}	1.1×10^{-2}	9.3×10^{-2}
	$\mathbf{1.9 \times 10^{-4}}$	$\mathbf{4.1 \times 10^{-4}}$	$\mathbf{4.8 \times 10^{-3}}$	$\mathbf{1.5 \times 10^{-2}}$	$\mathbf{6.4 \times 10^{-2}}$
0.95	5.6×10^{-5}	2.8×10^{-4}	4.5×10^{-4}	8.5×10^{-3}	8.3×10^{-2}
	$\mathbf{1.1 \times 10^{-4}}$	$\mathbf{3.2 \times 10^{-4}}$	$\mathbf{2.3 \times 10^{-3}}$	$\mathbf{8.7 \times 10^{-2}}$	$\mathbf{6.5 \times 10^{-2}}$

because MBH mass will dominate the orbital frequency and its evolution for an EMRI system, and the existence of charges will also influence the evolution of the frequency. In Fig. 6, we plot the mismatch as a function of δM for TQ, one can see that for given charges the threshold of the mismatch is satisfied only when $|\delta M|$ is much smaller than $M_\odot$, and it has already exceed the accuracy for the measurement of M which is about $\sim 10^{-6}$ relative to M [32]. Thus, we can conclude that the presence of charges will not affect the parameter estimation precision of the mass of the central BH, if we cannot distinguish whether it is charged or not.

B. Constraint on charges

In this subsection, we perform the parameter estimation for the charges Q and q using the FIM method. Note that in this subsection to characterize the effects of the charges on the parameter estimation, the cutoff of the inspiral is chosen to be the ISCO, such that the charged and uncharged waveforms have different cutoff frequencies. It should be noted that charges indeed influence on the radius of ISCO and parameter estimation is subjected with the cutoff frequency [33]; thus, it is necessary to assess quantitatively the effects of charges on parameter estimation. We also

choose the luminosity to be 1 Gpc and do not normalize the SNR, since it will significantly influence the parameter estimation accuracy.

First of all, by taking the central values of the charges to be zero, we can study the effects of the mass M and the spin parameter a on the constraints for the charges. The constraints for Q and q measured by LISA and TQ, are showed in Tables I and II, respectively. One can see that in the chosen range for M and a, constraints achievable for Q and q are in the range of 10^{-1}–10^{-5}. Overall, The capability for TQ and LISA are almost on the same level, while LISA is a little bit better, since the generated GWs are in the lower frequency band. The constraints will be better for an EMRI system with lighter mass and higher spin.

We then study the effects of the charges on the parameter estimation precision. From Fig. 7, we can find that the relative errors for both Q and q decrease with the MBH charge Q. This can be explained by the fact that the ISCO radius r_{ISCO} of the charged CO decreases with the charge of the KN BH, as shown in bottom pane of Fig. 1. Smaller r_{ISCO} means the CO will orbiting more cycles around the KN MBH, then such EMRI event will have higher SNR. Similar phenomenon has been found for the strong effect on the parameter estimation from the choices of the waveform cutoff [30,33]. Besides, we can see that the
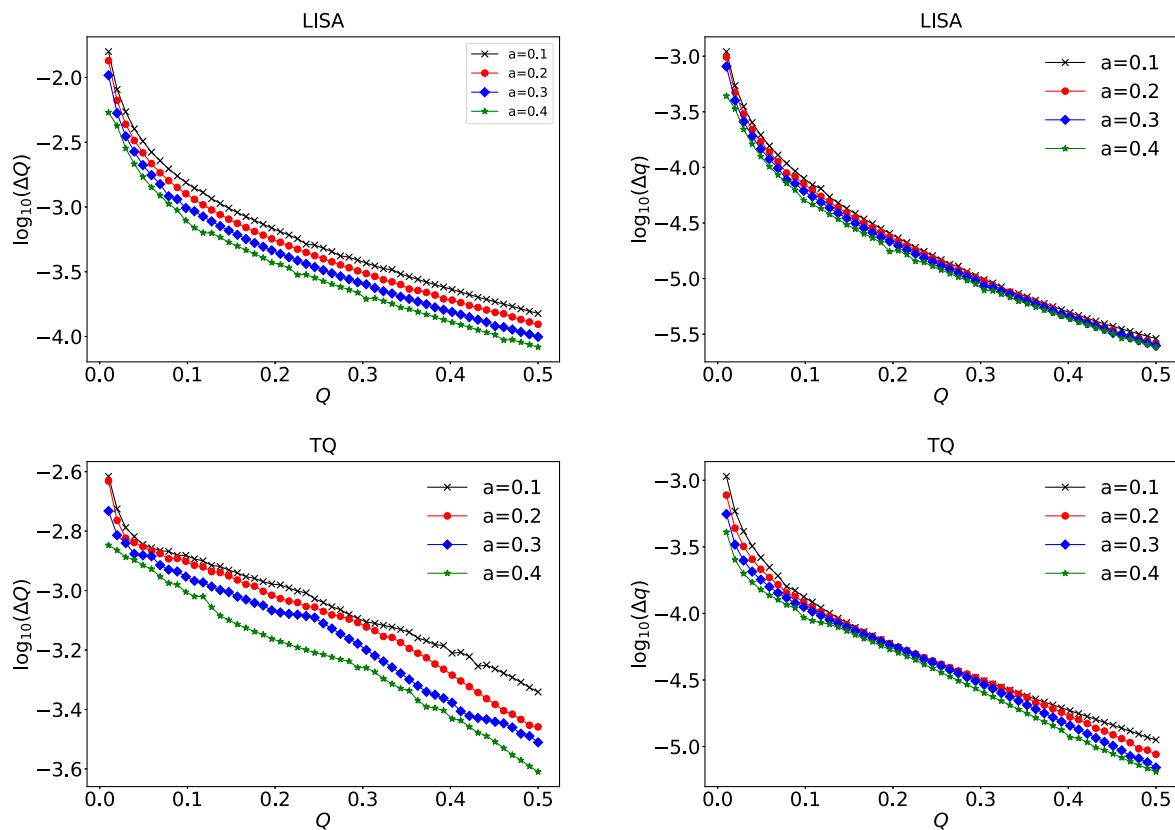

FIG. 7. PE accuracy for charge parameter, $\log_{10}(\Delta Q)$ (the left panels) and $\log_{10}(\Delta q)$ (the right panels), as a function of MBH charge Q for LISA (the top panels) and TQ (the bottom panels), respectively. The charge of CO is set as $q = 0$. The other parameters keep same with the previous configurations in Fig. 3.
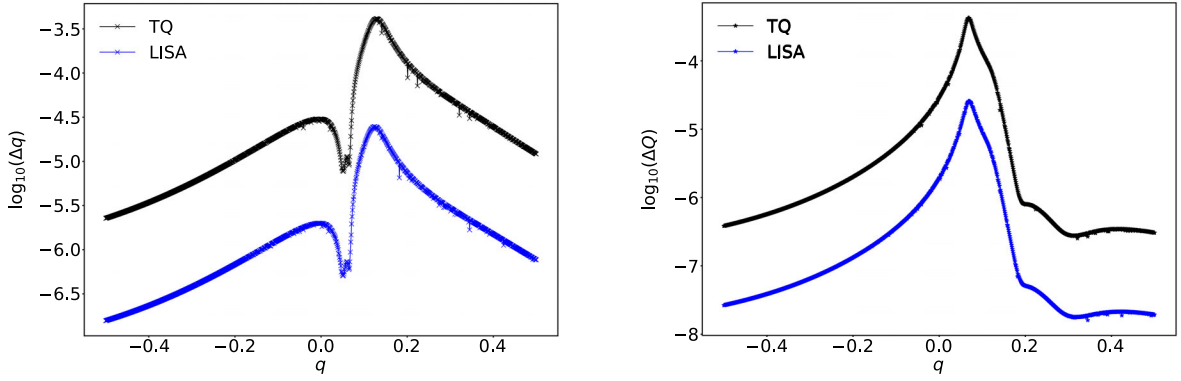
FIG. 8. PE accuracy for charge parameter, $\log_{10}(\Delta q)$ (the left panel) and $\log_{10}(\Delta Q)$ (the right panel), as a function of CO charge q for LISA (the red circle) and TQ (the black cross), respectively. The charge and spin of MBH is set as $Q = 0.1$ and $a = 0.6$, respectively. The other parameters keep same with the previous configurations in Fig. 3.

larger the MBH spin the higher the estimation precision the charges of the waveforms can have. The effects of the CO charge q on the relative errors for both Q and q are more complicated. As shown in Fig. 8, we can see that the parameter estimation overall increase when $|q|$ is large, which could be explained by the enhancement of the electric force between the CO and the MBH in this case. However, the unsmooth behavior of $\log(\Delta q)$ at $0 < q < 0.2$ is unclear.

V. CONCLUSION

In this paper, we derived the charged version of the AK waveform by considering the spiral of a charged stellar-mass compact object into a charged massive black hole. The latter is described by the Kerr-Newman metric. From the equations of motion of the charged CO in the KN spacetime, we computed the three fundamental frequencies in the weak-field regime, from which the equations describing the evolution of the perihelion precession and the orbital plane precession were obtained. Moreover, the evolution equations of the radial orbital frequency and the eccentricity were derived from the energy flux and the angular momentum flux due to the gravitational radiation and electromagnetic radiation. Combine these leading order corrected equations with those higher-order PN equations in the original AK model, the complete orbital evolution equations were obtained.

We found that the correction of charge on AK waveform is evidently different from the original AK waveform, as long as the EMRI system carry a tiny amount of charges. This is supported quantitatively by calculating the mismatch of the two different AK waveforms with respect to TianQin and LISA. We then performed the parameter estimation precision for the charges Q and q and found that space borne detectors can measure them with accuracy to the level of 10^{-5} under suitable scenarios. This is almost the level of the upper limit caused by different neutralized mechanisms [70], and far beyond the level if some charged

mechanisms exist. Moreover, we studied the effects of Q and q on the parameter estimation precision of themselves. We found that the effects on the parameter estimation precision from Q are almost dominated by the changing of ISCO, and for the parameter estimation precision from q, the behavior at large q may due to the enhancement of the electric force between the CO and the MBH.

The AK model employed in this work is known to be insufficiently accurate in the strong-field regime. Instead, the numerical kludge (NK) model [36] is more accurate but with a slightly expensive computational cost. Therefore, it would be interesting to consider the charged version of the NK model, where the trajectory of CO is obtained by solving the equations of motion strictly and the GW waveform is still calculated with the quadrupole-octupole formula. The last piece of the NK model is using semi-analytic fits to strong-field radiation emission to describe inspiral, which seems not easy for the charged EMRI system. This is because the strong-field radiation emission is governed by the Teuskolsky equations and the counterpart in the charged case is a set of coupled partial differential equations, which is much more harder to handle.

ACKNOWLEDGMENTS

[1] J. D. Bekenstein, arXiv:gr-qc/9605059.
[2] P. T. Chrusciel, J. Lopes Costa, and M. Heusler, Living Rev. Relativity **15**, 7 (2012).
[3] E. T. Newman, R. Couch, K. Chinnapared, A. Exton, A. Prakash, and R. Torrence, J. Math. Phys. (N.Y.) **6**, 918 (1965).
[4] G. W. Gibbons, Commun. Math. Phys. **44**, 245 (1975).
[5] R. D. Blandford and R. L. Znajek, Mon. Not. R. Astron. Soc. **179**, 433 (1977).
[6] R. M. Wald, Phys. Rev. D **10**, 1680 (1974).
[7] J. Levin, D. J. D'Orazio, and S. Garcia-Saenz, Phys. Rev. D **98**, 123002 (2018).
[8] J. Preskill, Annu. Rev. Nucl. Part. Sci. **34**, 461 (1984).
[9] L. Liu, Ø. Christiansen, Z. K. Guo, R. G. Cai, and S. P. Kim, Phys. Rev. D **102**, 103520 (2020).
[10] J. W. Moffat, J. Cosmol. Astropart. Phys. 03 (2006) 004.
[11] J. W. Moffat, Phys. Lett. B **763**, 427 (2016).
[12] V. Cardoso, C. F. B. Macedo, P. Pani, and V. Ferrari, J. Cosmol. Astropart. Phys. 05 (**2016**) 054; 04 (2020) E01.
[13] A. F. Zakharov, Phys. Rev. D **90**, 062007 (2014).
[14] M. Zajaček, A. Tursunov, A. Eckart, and S. Britzen, Mon. Not. R. Astron. Soc. **480**, 4408 (2018).
[15] H. T. Wang, P. C. Li, J. L. Jiang, Y. M. Hu, and Y. Z. Fan, Eur. Phys. J. C **81**, 769 (2021).
[16] G. Bozzola and V. Paschalidis, Phys. Rev. Lett. **126**, 041103 (2021).
[17] G. Bozzola and V. Paschalidis, Phys. Rev. D **104**, 044004 (2021).
[18] H. T. Wang, S. P. Tang, P. C. Li, and Y. Z. Fan, Phys. Rev. D **104**, 104063 (2021).
[19] P. C. Li, T. C. Lee, M. Guo, and B. Chen, Phys. Rev. D **104**, 084044 (2021).
[20] P. K. Gupta, T. F. M. Spieksma, P. T. H. Pang, G. Koekoek, and C. V. Broeck, Phys. Rev. D **104**, 063041 (2021).
[21] G. Carullo, D. Laghi, N. K. Johnson-McDaniel, W. Del Pozzo, O. J. C. Dias, M. Godazgar, and J. E. Santos, Phys. Rev. D **105**, 062009 (2022).
[22] B. P. Abbott *et al.* (LIGO Scientific and Virgo Collaborations), Phys. Rev. X **9**, 031040 (2019).
[23] R. Abbott *et al.* (LIGO Scientific and Virgo Collaborations), Phys. Rev. X **11**, 021053 (2021).
[24] O. J. C. Dias, M. Godazgar, J. E. Santos, G. Carullo, W. Del Pozzo, and D. Laghi, Phys. Rev. D **105**, 084044 (2022).
[25] J. Bao, C. Shi, H. Wang, J. d. Zhang, Y. Hu, J. Mei, and J. Luo, Phys. Rev. D **100**, 084024 (2019).
[26] P. Amaro-Seoane, Living Rev. Relativity **21**, 4 (2018).
[27] P. Amaro-Seoane, arXiv:2011.03059.
[28] J. Mei *et al.* (TianQin Collaboration), Prog. Theor. Exp. Phys. **2021**, 05A107 (2021).
[29] P. Amaro-Seoane *et al.* (LISA Collaboration), arXiv: 1702.00786.
[30] S. Babak, J. Gair, A. Sesana, E. Barausse, C. F. Sopuerta, C. P. L. Berry, E. Berti, P. Amaro-Seoane, A. Petiteau, and A. Klein, Phys. Rev. D **95**, 103012 (2017).
[31] C. P. L. Berry, S. A. Hughes, C. F. Sopuerta, A. J. K. Chua, A. Heffernan, K. Holley-Bockelmann, D. P. Mihaylov, M. C. Miller, and A. Sesana, arXiv:1903.03686.
[32] H. M. Fan, Y. M. Hu, E. Barausse, A. Sesana, J. d. Zhang, X. Zhang, T. G. Zi, and J. Mei, Phys. Rev. D **102**, 063016 (2020).
[33] T. G. Zi, J. D. Zhang, H. M. Fan, X. T. Zhang, Y. M. Hu, C. Shi, and J. Mei, Phys. Rev. D **104**, 064008 (2021).
[34] A. Pound and B. Wardell, arXiv:2101.04592.
[35] L. Barack and C. Cutler, Phys. Rev. D **69**, 082005 (2004).
[36] S. Babak, H. Fang, J. R. Gair, K. Glampedakis, and S. A. Hughes, Phys. Rev. D **75**, 024005 (2007); **77**, 04990(E) (2008).
[37] A. J. K. Chua, C. J. Moore, and J. R. Gair, Phys. Rev. D **96**, 044005 (2017).
[38] A. J. K. Chua, M. L. Katz, N. Warburton, and S. A. Hughes, Phys. Rev. Lett. **126**, 051102 (2021).
[39] M. L. Katz, A. J. K. Chua, L. Speri, N. Warburton, and S. A. Hughes, Phys. Rev. D **104**, 064047 (2021).
[40] E. Barausse, L. Rezzolla, D. Petroff, and M. Ansorg, Phys. Rev. D **75**, 064026 (2007).
[41] C. F. Sopuerta and N. Yunes, Phys. Rev. D **80**, 064006 (2009).
[42] P. Pani, V. Cardoso, and L. Gualtieri, Phys. Rev. D **83**, 104048 (2011).
[43] J. Gair and N. Yunes, Phys. Rev. D **84**, 064016 (2011).
[44] P. Canizares, J. R. Gair, and C. F. Sopuerta, Phys. Rev. D **86**, 044010 (2012).
[45] N. Yunes, P. Pani, and V. Cardoso, Phys. Rev. D **85**, 102003 (2012).
[46] C. J. Moore, A. J. K. Chua, and J. R. Gair, Classical Quantum Gravity **34**, 195009 (2017).
[47] M. Liu and J. d. Zhang, arXiv:2008.11396.
[48] C. Zhang and Y. Gong, Phys. Rev. D **105**, 124046 (2022).
[49] P. C. Peters and J. Mathews, Phys. Rev. **131**, 435 (1963).
[50] P. C. Peters, Phys. Rev. **136**, B1224 (1964).
[51] E. Hackmann and H. Xu, Phys. Rev. D **87**, 124030 (2013).
[52] B. Carter, Phys. Rev. **174**, 1559 (1968).
[53] W. Schmidt, Classical Quantum Gravity **19**, 2743 (2002).
[54] Y. Mino, Phys. Rev. D **67**, 084027 (2003).
[55] S. Drasco and S. A. Hughes, Phys. Rev. D **69**, 044015 (2004).
[56] R. Fujita and W. Hikida, Classical Quantum Gravity **26**, 135002 (2009).
[57] Another usual orbital inclination angle is defined in terms of the Carter constant by $\cos \lambda_I = \frac{L_z}{\sqrt{C+L_z^2}}$, which in the limit $a \to 0$ becomes $\cos \lambda_I = L_z/L$ and one has $\theta_{tp} + (\text{sgn} L_z)\lambda_I = \pi/2$, where L is the total orbital angular momentum.
[58] Here we use the convention in [59], where the Lagrangian of the electromagnetic field is $\mathcal{L} = -\frac{1}{16\pi}F_{\mu\nu}F^{\mu\nu} + A_\mu J^\mu$ and the equation of motion is $\nabla_\mu F^{\mu\nu} = -4\pi J^\mu$.
[59] L. D. Landau and E. M. Lifshitz, *The Classical Theory of Fields* (Pergamon Press, New York, 1971).
[60] L. Liu, Z. K. Guo, R. G. Cai, and S. P. Kim, Phys. Rev. D **102**, 043508 (2020).
[61] Ø. Christiansen, J. Beltrán Jiménez, and D. F. Mota, Classical Quantum Gravity **38**, 075017 (2021).
[62] L. Liu, Ø. Christiansen, Z. K. Guo, R. G. Cai, and S. P. Kim, Eur. Phys. J. C **81**, 1048 (2021).
[63] L. Liu and S. P. Kim, J. Cosmol. Astropart. Phys. 03 (2022) 059.
[64] See Supplemental Material at http://link.aps.org/supplemental/10.1103/PhysRevD.107.023005 for the explicit derivation of these expressions using *Mathematica*.

[65] C. Cutler and E. E. Flanagan, Phys. Rev. D **49,** 2658 (1994).

[66] E. E. Flanagan and S. A. Hughes, Phys. Rev. D **57,** 4566 (1998).

[67] L. Lindblom, B. J. Owen, and D. A. Brown, Phys. Rev. D **78,** 124020 (2008).

[68] A. Buonanno, Y. b. Chen, and M. Vallisneri, Phys. Rev. D **67,** 024016 (2003); **74,** 029903(E) (2006).

[69] M. Vallisneri, Phys. Rev. D **77,** 042001 (2008).

[70] E. Barausse, V. Cardoso, and P. Pani, Phys. Rev. D **89,** 104059 (2014).